



RESEARCH ARTICLE

10.1002/2015JA021949

Key Points:

- Solar cycle impact on the topside ionosphere of Mars
- Scale height changes along the solar cycle as seen by Mars Express
- Possible induced magnetic field during low solar activity phase

Correspondence to:

B. Sánchez-Cano,
bscmdr1@leicester.ac.uk

Citation:

Sánchez-Cano, B., M. Lester, O. Witasse, S. E. Milan, B. E. S. Hall, P.-L. Blelly, S. M. Radicella, and D. D. Morgan (2015), Evidence of scale height variations in the Martian ionosphere over the solar cycle, *J. Geophys. Res. Space Physics*, 120, doi:10.1002/2015JA021949.

Received 23 SEP 2015

Accepted 21 NOV 2015

Accepted article online 24 NOV 2015

Evidence of scale height variations in the Martian ionosphere over the solar cycle

B. Sánchez-Cano¹, M. Lester¹, O. Witasse², S. E. Milan¹, B. E. S. Hall¹, P.-L. Blelly³, S. M. Radicella⁴, and D. D. Morgan⁵

¹Radio and Space Plasma Physics Group, Department of Physics and Astronomy, University of Leicester, Leicester, UK, ²ESTEC—Scientific Support Office, European Space Agency, Noordwijk, Netherlands, ³Institut de Recherche en Astrophysique et Planétologie, Toulouse, France, ⁴Abdus Salam International Centre for Theoretical Physics, Telecommunications/ICT for Development Laboratory, Trieste, Italy, ⁵Department of Physics and Astronomy, University of Iowa, Iowa City, Iowa, USA

Abstract Solar cycle variations in solar radiation create density changes in any planetary ionosphere, which are well established in the Earth's case. At Mars, however, the ionospheric response to such changes is not well understood. We show the solar cycle impact on the topside ionosphere of Mars, using data from the Mars Advance Radar for Subsurface and Ionospheric Sounding (MARSIS) on board Mars Express. Topside ionospheric variability during the solar cycle is analyzed through neutral scale height behavior. For moderate and high solar activity phases, the topside electron density profile is reproduced with an altitude-variable scale height. However, for the period of extremely low solar activity in 2008 and 2009, the topside was smaller in density than in the other phases of the solar cycle, and there is evidence that it could be reproduced with either a constant scale height or a height-variable scale height with lower electron density. Moreover, the ionosphere during this time did not show any apparent dependence on the EUV flux. This singular behavior during low solar activity may respond to the presence of an induced magnetic field which can penetrate to lower ionospheric altitudes than in other phases of the solar cycle due to the reduced thermal pressure. Numerical simulations of possible scenarios for two different solar cycle phases indicate that this hypothesis is consistent with the observations.

1. Introduction

Solar extreme ultraviolet (EUV) and X-ray photon flux are the main sources of ionization of a planetary atmosphere, especially in the inner solar system [e.g., Witasse *et al.*, 2008; Schunk and Nagy, 2009]. Consequently, long-term changes in solar flux due to the different phases of the solar cycle produce important changes in the dayside ionospheric structure of any solar system body.

At Mars, due to the lack of a global-scale internal magnetic field [Acuña *et al.*, 1999], the ionosphere is the main part of the upper atmosphere that interacts directly with the solar wind. In the last 40 years, many efforts have been made in order to understand the ionospheric response to the solar cycle [e.g., Zhang and Luhmann, 1992; Luhmann *et al.*, 1992; Fox *et al.*, 1996; Cravens, 1997; Mendillo *et al.*, 2006; Dubinin *et al.*, 2008; Withers, 2009; Lillis *et al.*, 2010; Akalin *et al.*, 2010; Withers *et al.*, 2014]. This resultant knowledge was limited initially to a few time intervals of data because of a lack of continuous missions, and an incomplete solar zenith angle (SZA) coverage due to planetary geometry constrains. The radio occultation experiment has been the most utilized method for deriving electron density profiles over time, but this technique only provides profiles for SZA between 45 and 127° in the so-called “occultation seasons” [Ness *et al.*, 2000], when the Mars and Earth positions are optimal for the radio science experiment. On the other hand, measurements of the temperature and composition of the ionosphere, until the arrival of Mars Atmosphere and Volatile Evolution (MAVEN) mission in 2014, came from only two single profiles measured by the Viking I and II landers with the retarding potential analyzer instrument [Hanson *et al.*, 1977]. Nevertheless, since 1997, Martian ionospheric understanding has been significantly improved because plasma measurements have been collected on a subseasonal timescale until the present date by Mars Global Surveyor (MGS) [Hinson *et al.*, 1999] and Mars Express [Chicarro *et al.*, 2004].

Most knowledge of an ionospheric response to differences in solar cycle inputs comes from the Earth. Although the details of atmospheric composition, planetary orbit, and planetary magnetization differ between Mars and Earth, we expect similarities in the general ionospheric response to solar activity. At Earth, the solar cycle drives large temperature differences in the terrestrial thermosphere, primarily due to

©2015. The Authors.

This is an open access article under the terms of the Creative Commons Attribution License, which permits use, distribution and reproduction in any medium, provided the original work is properly cited.

the variation of solar irradiance in the EUV and soft X-ray spectral range from 1 to 105 nm [Schunk and Nagy, 2009]. This temperature change causes an even larger density change in the upper thermosphere [Solomon *et al.*, 2011]. The same radiation is also responsible for the main ionization of Mars' atmosphere, and, in general, the thermosphere has a solar cycle-dependent behavior similar to Earth [e.g., Bougher *et al.*, 2015].

The response of Earth's ionosphere to periodic and nonperiodic changes of solar activity is well known and has been widely modeled. The International Reference Ionosphere (IRI) [Bilitza and Reinisch, 2008] and the NeQuick model [Nava *et al.*, 2008] are two examples of widely used empirical models. However, during the last solar minimum (end 2007 to end 2009), deficiencies in these models became apparent. EUV and X-ray radiation were exceptionally reduced compared with the previous solar minimum. As a result, the terrestrial thermosphere at high altitude was cooler and lower in density than expected [Solomon *et al.*, 2010, 2011, 2013], and in general, the low-density values measured either from space or from the ground were overestimated by the ionospheric models for local and global conditions [e.g., Sethi *et al.*, 2011; Adewale *et al.*, 2012; Klenzing *et al.*, 2013; Yue *et al.*, 2013].

The objective of this paper is to show the effect of the latest solar activity cycle on measured topside profiles of the ionosphere of Mars. Ionospheric variability over the solar cycle is analyzed through the neutral scale height, which gives information on the density distribution with altitude in the ionosphere, and in turn is related to thermal and transport processes. Furthermore, at Earth during the recent solar minimum the thermosphere became much colder and lower in density, although it is not clear if this was the case at Mars. For this reason, we look for evidence of similar or otherwise exceptional behavior as we analyze the response of Mars' ionosphere during this period of extreme low solar activity.

2. Data

The Mars Advanced Radar for Subsurface and Ionospheric Sounding (MARSIS) [Picardi *et al.*, 2004] on board Mars Express has been probing the topside ionosphere of Mars since June 2005, currently covering 10 years and with the best planetary coverage yet archived. When this instrument operates in the Active Ionospheric Sounding (AIS) mode, which occurs for short periods close to periapsis, the topside ionosphere is sounded [Gurnett *et al.*, 2005] following exactly the same physical principles of ionosondes on Earth [Sánchez-Cano *et al.*, 2012; Morgan *et al.*, 2013]. The final product is the topside electron density profile, which gives the electron density distribution with altitude from the main ionization peak to the spacecraft position.

Figure 1 shows the evolution of the 10 years of solar activity since the Mars Express spacecraft arrived at Mars. In Figure 1 (first and second rows), the sunspot number (SSN), the EUV proxy $F_{10.7}$, and the EUV solar irradiance measured by Thermosphere, Ionosphere, Mesosphere Energetics and Dynamics (TIMED)-Solar EUV Experiment (SEE) satellite [Woods and Eparvier, 2006] at a wavelength of 30.5 nm are plotted, all of them at 1 AU. This wavelength is the closest one obtained from TIMED to the solar 30.4 nm He-line, primarily responsible for the CO₂ photoionization at Mars [Kieffer *et al.*, 1992; Withers, 2009]. The EUV solar irradiance at 30.5 nm and the solar X-ray radiation measured by the GOES family of satellites [Grubb, 1975] have been scaled to the Mars heliocentric distance in Figure 1 (third and fourth rows, respectively). In order to analyze the ionospheric response to solar cycle changes, the AIS data set was split into four periods according to notable changes in the solar spectrum, as seen in Figure 1 by considering all the panels together. Period A corresponds to the moderate solar activity phase of the solar cycle in the declining phase of solar cycle 23, from the MARSIS radar deployment (mid-June 2005) to mid-September of 2007. As observed in Figure 1, all the parameters exhibit a lower level than the previous years (high solar activity), and a progressive reduction along the period. Period B corresponds to the low solar activity phase of the solar cycle 23/24, from mid-September 2007 to mid-September 2009. This period was characterized by a lower level of SSN, EUV, and $F_{10.7}$ index at 1 AU in comparison to Period A, being almost constant for these three parameters along the full period. The EUV at Mars, which depends on the orbit evolution, showed a general reduction in comparison to the former period, although the planetary orbit change did result in a 25% change during this interval. If Periods A and B are compared for the same heliocentric distances, e.g., the EUV minima and maxima of Periods A and B (farther and closer Mars-Sun position, respectively), the EUV flux is always smaller during the low solar activity phase. However, the most notable difference of this period is the almost permanent absence of measurable X-ray flux. Period C corresponds to the moderate solar activity in the ascending phase of the solar cycle 24, from mid-September 2009 to mid-February 2011. During this phase, every parameter

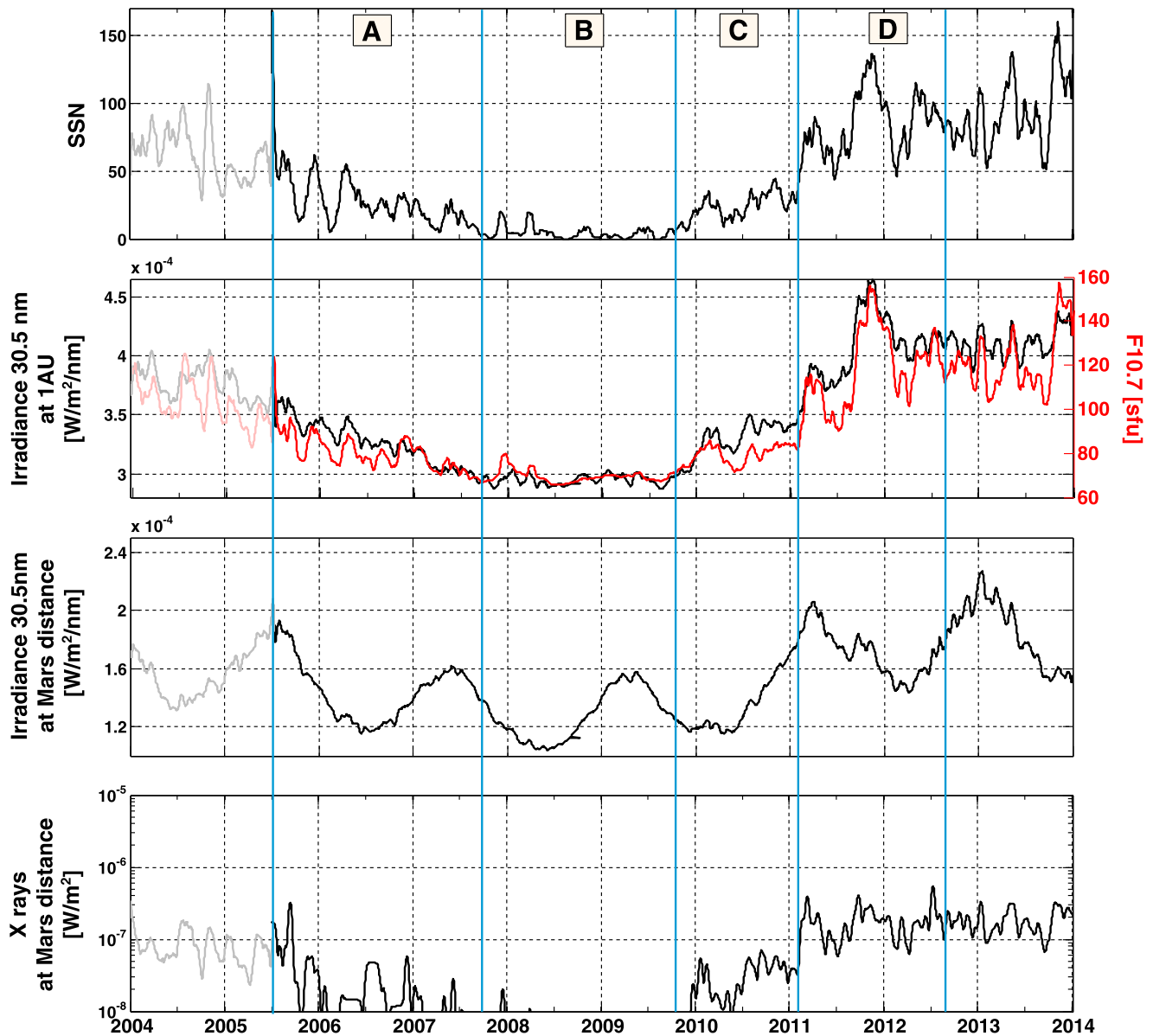


Figure 1. Solar cycle covered by Mars Express. (first row) Solar sunspot number (SSN). (second row) EUV solar irradiance at a wavelength of 30.5 nm (from TIMED-SEE satellite at 1 AU) and $F_{10.7}$ index as a proxy of the EUV radiation at 1 AU in red. (third row) EUV solar irradiance at 30.5 nm scaled to Mars distance. (fourth row) Solar X-rays measured by GOES family satellites scaled to Mars distance. The MARSIS operational time has been plotted in intense black/red color.

showed similar levels to those in Period A, with a progressive ascending trend along the period. This phase is the shortest of the four intervals. The main difference with respect to Period B is the notable increment of the X-ray flux to levels which are similar to Period A. Finally, Period D corresponds to the high activity phase of the solar cycle 24, from mid-February 2011 to June 2012. On average, all the parameters were higher in Period D than in the other three periods. The EUV flux at Mars reached the maximum of the four periods, and the level of X-ray flux was, on average, 1 order of magnitude larger than during Period C.

We have a number of selection criteria to identify the AIS profiles. The most general of these were described before by *Morgan et al.* [2013] and *Sánchez-Cano et al.* [2012, 2013] and are summarized here.

1. MARSIS needs to be working in AIS mode instead of subsurface mode.
2. Data have to be recorded in the dayside and with the specific SZA required by the study. This may seem trivial, but we note that Mars Express periapsis is in the nightside of the planet for large periods of time.

Table 1. Mean Neutral Scale Height of Each Solar Cycle Phase

SZA (deg)	Solar Cycle Period	Number Data/Number Orbits	Factor a (\pm SD)	H_n (km) at the Peak (\pm SD)	H_n (km) at 5 km (\pm SD)	H_n (km) at 10 km (\pm SD)	H_n (km) at 15 km (\pm SD)	H_n (km) at 20 km (\pm SD)	H_n (km) at 25 km (\pm SD)	H_n (km) at 30 km (\pm SD)	H_n (km) at 35 km (\pm SD)	H_n (km) at 40 km (\pm SD)
45–50	A	52/10	0.086 \pm 0.028	11.7 \pm 1.6	12.1 \pm 1.5	12.5 \pm 1.4	13.0 \pm 1.3	13.4 \pm 1.3	13.8 \pm 1.2	14.3 \pm 1.2	14.7 \pm 1.1	15.1 \pm 1.1
	B	153/12	0.069 \pm 0.022	11.1 \pm 1.8	11.5 \pm 1.7	11.8 \pm 1.7	12.2 \pm 1.6	12.5 \pm 1.5	12.9 \pm 1.5	13.2 \pm 1.4	13.6 \pm 1.4	13.9 \pm 1.3
	C	28/3	0.091 \pm 0.016	11.9 \pm 1.5	12.4 \pm 1.6	12.8 \pm 1.6	13.3 \pm 1.7	13.7 \pm 1.7	14.2 \pm 1.8	14.7 \pm 1.9	15.1 \pm 1.9	15.6 \pm 2.0
	D	27/7	0.093 \pm 0.013	13.0 \pm 2.3	13.4 \pm 2.3	13.9 \pm 2.2	14.4 \pm 2.2	14.8 \pm 2.2	15.3 \pm 2.2	15.7 \pm 2.2	16.2 \pm 2.2	16.7 \pm 2.2
50–55	A	186/27	0.091 \pm 0.029	10.9 \pm 2.0	11.3 \pm 1.9	11.8 \pm 1.9	12.3 \pm 1.9	12.7 \pm 1.8	13.2 \pm 1.8	13.6 \pm 1.8	14.1 \pm 1.8	14.5 \pm 1.8
	B	68/12	0.072 \pm 0.022	10.3 \pm 1.8	10.7 \pm 1.7	11.0 \pm 1.6	11.4 \pm 1.5	11.8 \pm 1.4	12.1 \pm 1.4	12.5 \pm 1.3	12.9 \pm 1.2	13.2 \pm 1.2
	C	26/4	0.098 \pm 0.016	11.6 \pm 1.7	12.2 \pm 1.7	12.6 \pm 1.7	13.1 \pm 1.7	13.6 \pm 1.7	14.1 \pm 1.7	14.6 \pm 1.7	15.0 \pm 1.7	15.5 \pm 1.7
	D	86/12	0.098 \pm 0.014	13.7 \pm 1.8	14.2 \pm 1.8	14.7 \pm 1.9	15.2 \pm 1.9	15.7 \pm 1.9	16.2 \pm 1.9	16.7 \pm 1.9	17.2 \pm 1.9	17.7 \pm 2.0

- The presence of local plasma harmonics [Andrews et al., 2013] is necessary to provide a measure of the local plasma density in order to derive the correct altitude of the electron density profile. This implies that Mars Express needs to be often below 500–600 km altitude. During the low solar activity phase, this altitude may even be reduced to 350–400 km (the periapsis is at ~275–300 km), resulting in the absence of local plasma harmonics.
- The whole ionospheric trace (including the lowest and the highest frequencies of the trace) has to be clearly recorded [see, e.g., Sánchez-Cano et al., 2013, Figure 2]. At the lowest-frequency part, the trace is difficult to track because of the noise and the overlap with the harmonic oscillations, and at the highest-frequency part, it is necessary to select a well-defined vertical signature of the trace in order to be sure that the values extracted are not affected by lack of definition in the ionogram, thereby minimizing the uncertainty of this parameter [Sánchez-Cano et al., 2013]. Moreover, atmospheric absorption often inhibits part of the full trace.

In addition to these four standard criteria, we have only selected profiles which occur over regions where no crustal magnetic field is present as the presence of the field makes the analysis of the ionograms more complex. Likewise, data from orbits affected by strong and/or fast solar wind, such as Coronal Mass Ejections (CMEs) are not considered because additional ionization sources (i.e., other than EUV) are enhanced at these times such as penetrating solar wind proton precipitation [Halekas et al., 2015], solar energetic particles [Lillis et al., 2012], and pickup oxygen ion precipitation [Leblanc et al., 2015]. Finally, we focus on two adjacent narrow ranges of SZA, 45–50° and 50–55°, as these provide us with the best distribution across all four periods of solar activity. These selection criteria result in 626 AIS topside electron density profiles over the two SZA ranges. These profiles are distributed in each solar cycle phase as specified in Table 1. We note that the amount of available AIS profiles that fulfill the above criteria depends on the time length of each solar phase, on the time slots that MARSIS was working in AIS mode, and on the planetary coverage described by the Mars Express orbit evolution.

In order to assess the impact of the planetary orbital distance in the EUV spectrum, we show the topside total electron content (TEC) estimated from the profiles used in this study as a function of the EUV solar irradiance at 30.5 nm scaled to Mars, for each phase of the solar cycle (Figure 2). The topside TEC is a useful parameter to evaluate the amount of ionization within the atmosphere and is obtained by a direct integration of the topside density profile in altitude [Sánchez-Cano et al., 2015]. On average, a topside TEC reduction of $0.2 \cdot 10^{16} \text{ m}^{-2}$ during period B, and an enhancement of $0.4 \cdot 10^{16} \text{ m}^{-2}$ during period D, both with respect to the moderate activity periods (A and C), can be inferred from the figure. In more detail, for EUV fluxes lower than $1.3 \cdot 10^{-4} \text{ W/m}^2$, the average topside TEC of Period B was $0.2 \cdot 10^{16} \text{ m}^{-2}$ smaller than Period A for both SZA intervals, and Period A was $0.1 \cdot 10^{16} \text{ m}^{-2}$ smaller than Period C for both SZA intervals. For EUV fluxes higher than $1.3 \cdot 10^{-4} \text{ W/m}^2$ and lower than $1.6 \cdot 10^{-4} \text{ W/m}^2$, the average topside TEC of Period B was again $0.2 \cdot 10^{16} \text{ m}^{-2}$ smaller than Period A for SZA 50–55°, while for EUV fluxes higher than $1.6 \cdot 10^{-4} \text{ W/m}^2$, the average topside TEC of Period D was $0.4 \cdot 10^{16} \text{ m}^{-2}$ higher than Period A for both SZA intervals. Moreover, a significant increasing trend with increasing EUV solar irradiance is found when both moderate solar activity periods (A and C) and the high solar phase (Period D) are considered, while the low solar activity phase (Period B) shows an almost constant behavior with the EUV flux. This figure demonstrates that the Martian ionospheric behavior, for the same level of solar activity, was clearly different depending on the solar cycle phases, especially for the low solar activity phase.

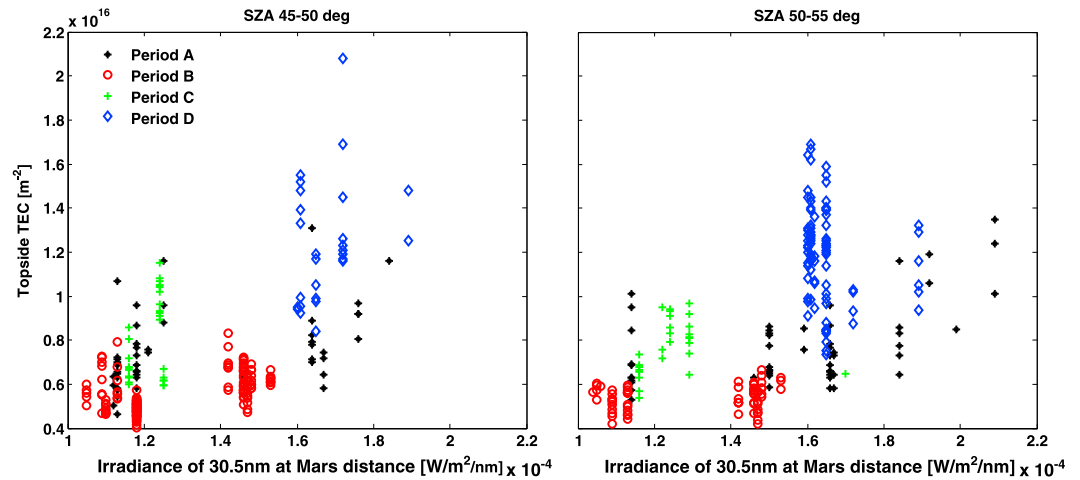


Figure 2. Topside total electron content (TEC) of measured profiles in relation to the EUV solar irradiance at 30.5 nm scaled to Mars (left) for SZA = 45–50° and (right) for SZA = 50–55°. Each phase of the solar cycle is represented with a different color and shape as shown in the figure.

3. Electron Density and Neutral Scale Height Variation With Solar Cycle

The atmospheric and ionospheric scale heights are two of the main parameters that define the electron density profile. The scale height measures the height range in which the plasma and neutral density change by a factor of e , such that these parameters control the shape of the vertical density profile [Belehaki et al., 2006].

For a medium in hydrostatic equilibrium and with constant temperature, the scale height, H , is defined as

$$H = \frac{K_B T}{mg} \tag{1}$$

where m is the mean molecular mass of the medium, T is its temperature, g is the acceleration due to the gravity of the planet at ionospheric altitudes, and K_B is the Boltzmann constant. The scale height can describe the altitude distribution of the neutral and plasma components of the ionosphere, depending on which mass, m , and temperature, T , are considered: that is, for the atmospheric scale height, the temperature of the neutral components and the mass of CO_2 are used, and for the ionospheric scale height, the temperature of the ions plus electrons and the mass of O_2^+ for the ion mass are used. This work focuses on the neutral scale height because this is appropriate for the Chapman formulation that describes the shape of the electron density profile at Mars [Gurnett et al., 2005]. However, a similar result is expected if the plasma population is considered. Since only small changes in composition due to the solar cycle are expected in the photochemical region (hydrostatic region) [e.g., Fox et al., 1996, Figure 1], the neutral scale height differences are expected to be directly dependent on the temperature variations.

We use profiles that have the same SZA, but the heliocentric distance and therefore the incident solar flux are different for each particular case and the profiles cannot be directly compared. Therefore, we normalize the profiles using

$$\frac{N}{N_o} \text{ and } \frac{h - h_o}{H_o} \tag{2}$$

where N and h are the density and altitude along the profile, respectively; N_o and h_o are the density and altitude values of the electron density peak of each profile, respectively; and H_o is the neutral scale height of each profile in the peak region. H_o is calculated by numerically fitting each individual profile to an α -Chapman layer with a scale height which varies with height as described by equation (3)

$$H = H_o + a(h - h_o) \tag{3}$$

where a is the normalization factor which reflects the degree to which H depends on h . At the end of the process, $H(h)$, H_o , and a are acquired for each AIS profile [see also Sánchez-Cano et al., 2013]. Figures 3

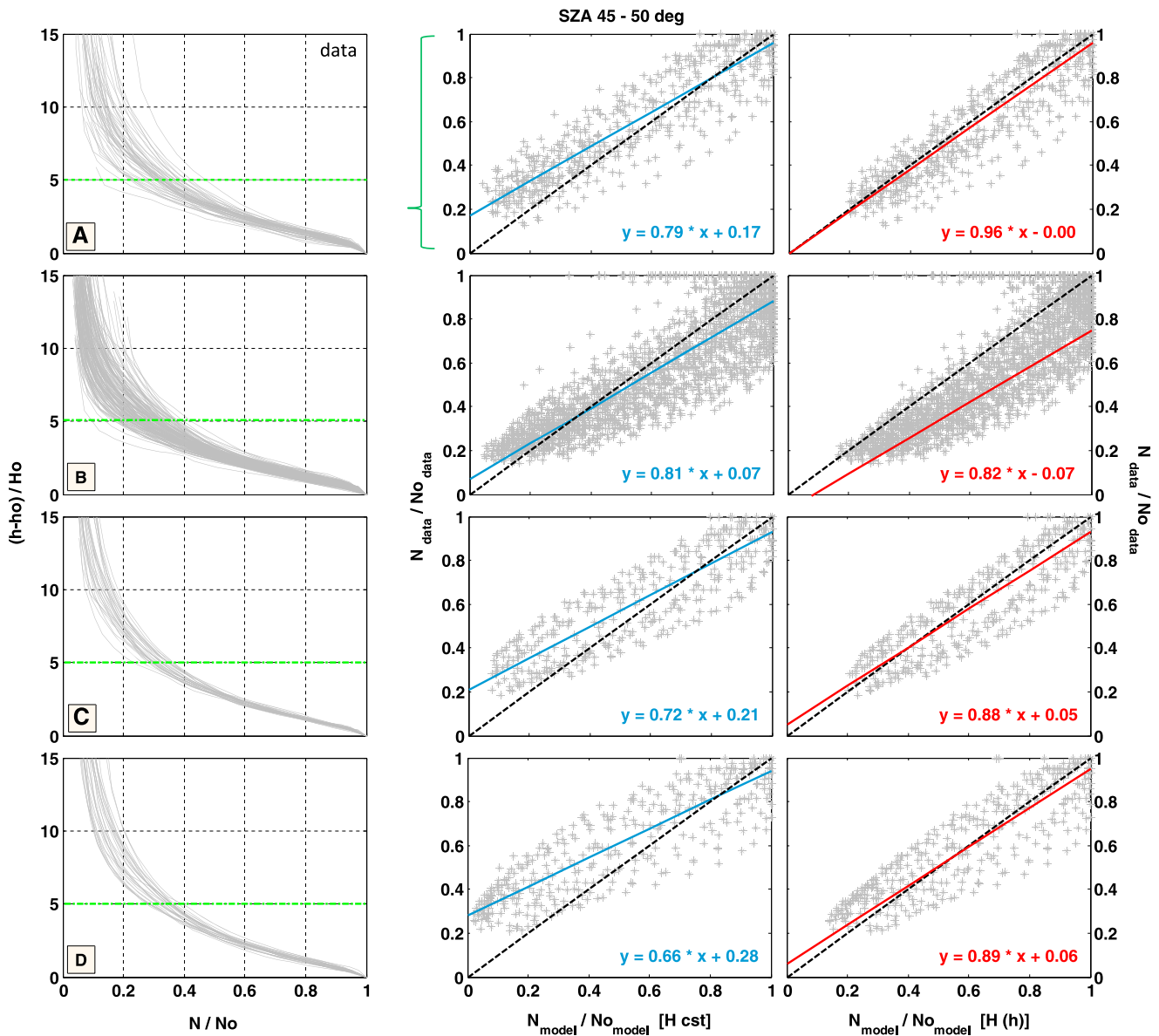


Figure 3. (left column) AIS-normalized electron density topside for each solar cycle phase (in rows) within SZA = 45–50°. (middle and right columns) Relationship between the normalized density observations of the photochemical region (data below green line in Figure 3, left column) and the model reference density with constant scale height, H (Figure 3, middle column) and with an altitude-variable H (Figure 3, right column). In each panel, the relation 1:1 is indicated with a black dashed line and the current linear best fit with a blue (Figure 3, middle column) or red (Figure 3, right column) solid line. The equations correspond to the best fit of each panel, y being the parameter of the vertical axis and x of the horizontal one.

(left column) and 4 (left column) show the normalized AIS topside profiles selected for this study for the SZA ranges 45–50° and 50–55°, respectively. Although the profiles may look similar for the four cases with this representation, there are clear differences in density that will be analyzed later. Table 1 shows the averaged H of the profiles for different altitudes and for each phase of the solar cycle in the photochemical region (up to about 170 km, i.e., below the horizontal green line in Figures 3 and 4). For both SZA intervals, all periods have a similar variation of H with altitude as indicated by the parameter, a , except the period of low solar activity (Period B) which has the smallest degree of variation. Based on a Student’s t test, the mean value of the parameter a of Period B is statistically significantly different, at the 99% or above, with respect to the other three Periods in both SZA intervals.

In order to evaluate quantitatively the differences of the density profiles in altitude for each solar cycle period and, in particular, to assess the degree of variation of the ionospheric density during the low solar activity

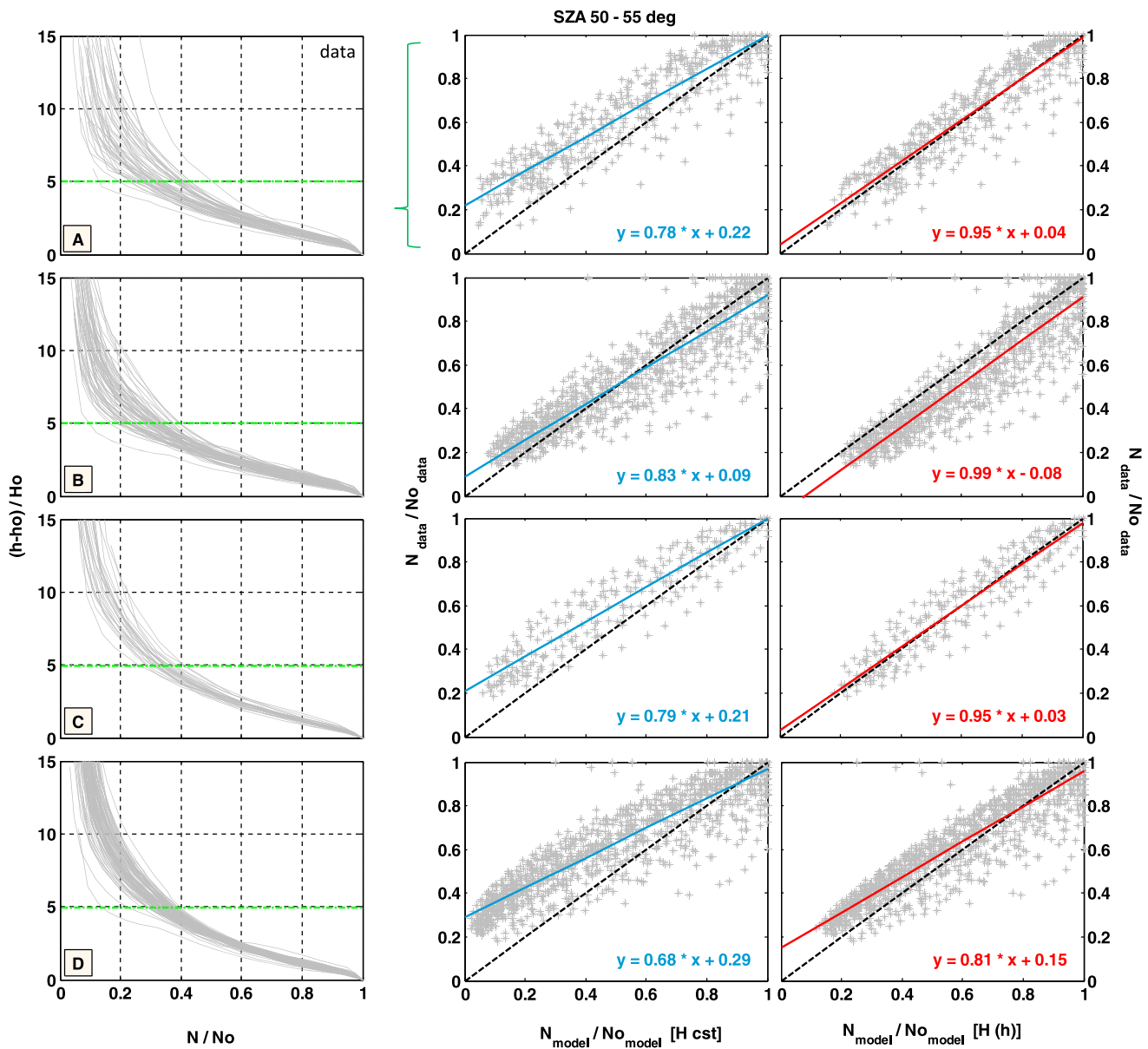


Figure 4. Same as Figure 3 but for SZA = 50–55°.

phase (Period B), the observations from the photochemical region (below 170 km) have been compared with a reference ionosphere, which is the empirical model NeMars based on MARSIS AIS data [Sánchez-Cano et al., 2013]. This model is based on the Chapman formulation and describes the shape of the modeled electron density topside with a scale height H that depends linearly on altitude (similar to equation (3)) and with an exponential SZA dependence. Therefore, the model does not consider any variation of H with solar activity or with the different phases of the solar cycle and can be used as a reference for this study. In Figures 3 (middle and right columns) and 4 (middle and right columns), the relationship between the normalized densities of the observations ($N_{data}/N_{o_{data}}$) and the normalized model reference density ($N_{model}/N_{o_{model}}$) is plotted, where a constant scale height, H , has been used in the middle column (i.e., the altitude dependence of H in the model was removed) and an altitude-varying H in the right column (i.e., the altitude dependence of H in the model was kept). In each panel, the relation 1:1 is indicated with a black dashed line and the current linear best fit with a blue (middle column) or red (right column) solid line. The equations of these best fits are included in each subpanel. In general, Periods A, C, and D show a closer behavior to the Chapman model reference when an altitude-variable H is considered instead of a constant value. For the high solar

activity period (Period D), the density is slightly larger than the reference altitude-variable H for the SZA range 50–55° (Figure 4, right column). These results are in accordance with Table 1, in particular at higher altitudes (at 0.2–0.6 normalized density). However, for periods A, C, and D the relationship between the observed and reference values when a constant H is considered is poor. This is evidence that the altitude-variable H is more appropriate for describing the ionosphere during these periods.

For Period B (low solar activity), the density behavior is closer to the reference one when a constant H is considered for both SZA intervals (Figures 3, middle column, and 4, middle column), while a clear reduction in density is observed for almost all the data points with respect to the relation 1:1 in the altitude-variable case (Figures 3, right column, and 4, right column). The lines of best fits in the altitude-variable case (Figures 3, right column, and 4, right column) do follow a simple trend but with an offset below that trend. However, the constant scale height profile provides a closer fit to the simple trend. The ionospheric density may have responded to a linear altitude-variable H with a smaller rate of variation in altitude (as the red fit indicates), or simply the scale height becomes constant (as the blue fit indicates), which is not the case in other phases of the solar cycle. We can, however, conclude that during Period B, a notable topside electron density reduction with altitude took place. As mentioned above, this period was characterized by an especially prolonged solar minimum, which was deeper than the previous solar minimum: the EUV radiation was extremely reduced from end 2007 to end 2009, and detectable X-rays were practically absent (Figure 1). We believe that the ionosphere and thermosphere may have been cooler, and therefore, an overall reduction of the scale height is found.

We note that although changes in the neutral atmosphere inferred from electron density variability have been previously analyzed [e.g., *Bougher et al.*, 2001], our analysis shows that solar cycle variations can be identified in neutral scale height changes in the topside ionosphere of Mars, which has never been noted before with observational data.

4. Possible Induced Magnetic Field in the Upper Ionosphere

The low solar activity phase resulted in a general reduction in the density of the topside ionosphere of Mars. Generally, topside reductions are associated with induced magnetic fields of solar wind origin at the top of the ionosphere. This has been extensively analyzed with different data sets and modeling. For example, *Russell and Vaisberg* [1983] show a combination of magnetic field and electron density profiles from the Pioneer Venus Orbiter (PVO) mission to Venus, where the stronger the magnetic field is at the top of the ionosphere, the deeper it penetrates and a more compressed ionosphere (characterized by a lower scale height) is found. In the case of Mars, *Morel et al.* [2004] modeled the ionospheric behavior under differing magnetic field magnitudes at the top of the ionosphere and found that the magnetic field can influence the electron density profile of the Martian ionosphere [see *Morel et al.*, 2004, Figure 6]. Similarly, during a period of numerous coronal mass ejections a clear lower topside scale height was seen at Mars using Mars Express radio occultation data [*Withers et al.*, 2012, Figure 2A].

It could be possible that for the minimum solar cycle condition, the Martian ionosphere was in most of the cases weak enough to allow the penetration of an induced magnetic field from the solar wind at the uppermost ionosphere. We do not mean that the magnitude of the induced magnetic field was greater during that period, but the ionosphere was smaller in extent, and therefore, an induced magnetic field could penetrate to lower altitudes, resulting in a less extended photochemical region. To evaluate this possible scenario, numerical simulations are required. The numerical/fluid model TRANSMARS has been used for this task. This model was built from the models existing for the Earth [e.g., *Lilensten et al.*, 1989; *Blelly et al.*, 1996; *Diloy et al.*, 1996; *Witasse et al.*, 1999; *Culot et al.*, 2004; *Simon et al.*, 2005] and adapted for Mars [*Witasse*, 2000; *Witasse et al.*, 2002, 2003; *Morel et al.*, 2004; *Leblanc et al.*, 2008; *Simon et al.*, 2009]. It is a one-dimensional kinetic-fluid coupled model covering the altitude range 100–500 km. The kinetic part is a stationary Boltzmann approach, which computes the energetic electron flux. The ionizing source may be either the incoming solar wind electrons or photoelectrons. In this latter case, a photoproduction equation is also solved. The fluid part is an eight moment time-dependent model that solves the transport equations of different charged species e^- , CO_2^+ , O_2^+ , O^+ , H^+ , NO^+ , and N_2^+ . The formalism allows the computation of an equation for the induced magnetic field, similarly to *Shinagawa and Cravens* [1989]. The main inputs of the model are the neutral atmosphere, the solar flux in the EUV range [*Richards et al.*, 1994], and the

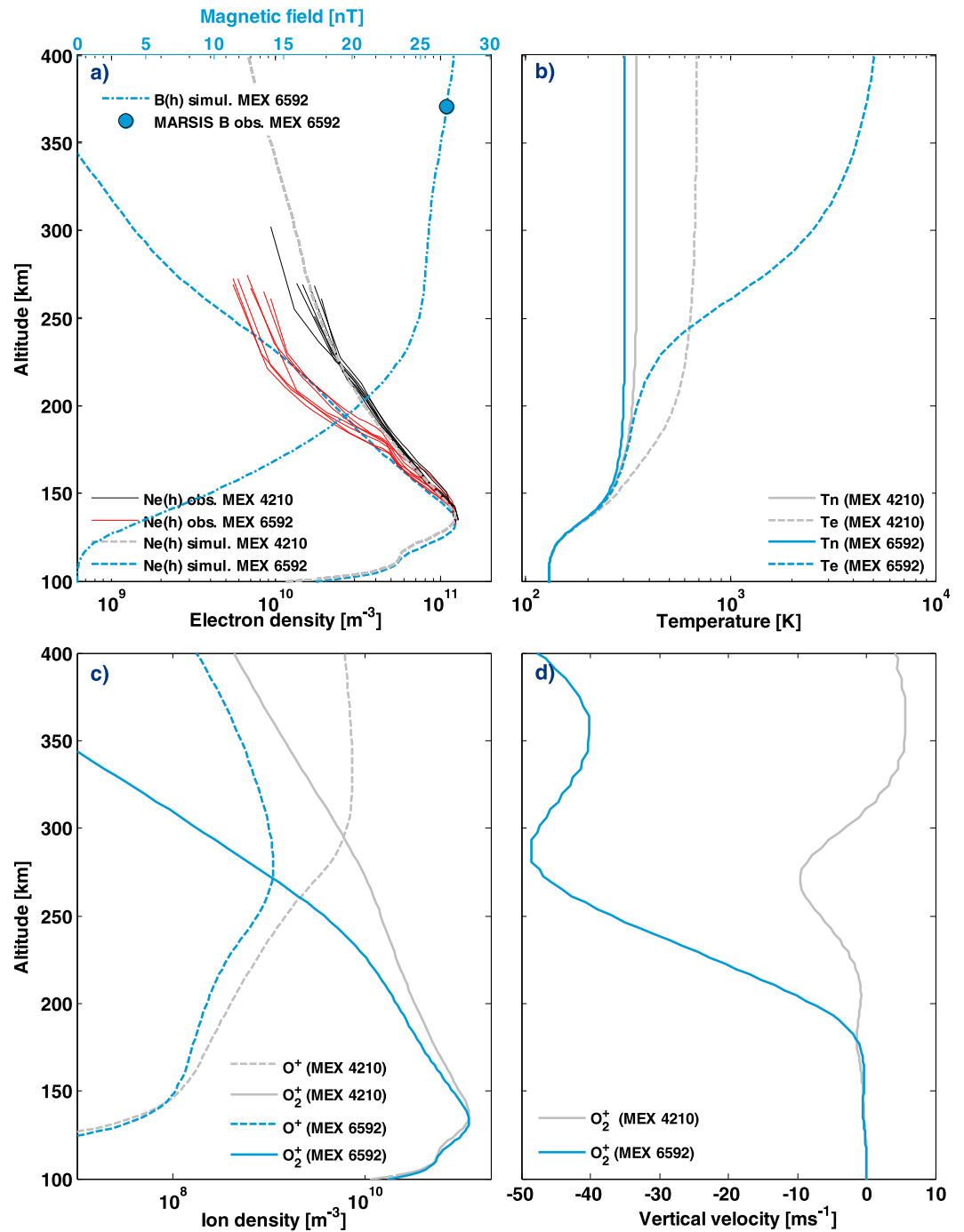


Figure 5. (a) Bottom x axis: the measured electron density profiles of orbit 4210, Period A (in black), and of orbit 6592, Period B (in red). Simulated electron density profiles in dashed lines. Top x axis: induced magnetic field profile from the simulation of orbit 6592 in dash-dotted line. MARSIS magnetic field observation in a circle for orbit 6592. A value of 0 nT has been considered for orbit 4210. (b) Neutral and electron temperatures profiles derived from the simulations. (c) Ion density, O^+ and O_2^+ , profiles derived from the simulations. (d) Vertical O_2^+ ion velocities derived from the simulations.

energetic electron precipitation. The main outputs are, as a function of altitude, the energetic ionizing electron fluxes, the primary and secondary ion production rates, the ion and neutral excitation production rates, the ion densities, the ion and electron velocities, and the ion and electron temperatures.

A case study is presented in Figure 5, where 14 AIS profiles are analyzed from two different orbits belonging to different phases of the solar cycle, but with similar solar activity and planetary and spacecraft orbital

Table 2. Parameters of the Simulations of Figure 5

	MEX ^a Orbit 4210	MEX Orbit 6592
<i>h = 135 km (Peak)</i>		
Electron density (m ⁻³)	1.2 · 10 ¹¹	1.2 · 10 ¹¹
Neutral temperature (K)	200.8	200.5
Electron temperature (K)	206.8	202.8
Magnetic field (nT)	0	5.5
CO ₂ density (kg m ⁻³)	2.7 · 10 ¹⁶	2.1 · 10 ¹⁶
O ₂ density (kg m ⁻³)	9.8 · 10 ¹³	9.8 · 10 ¹³
O density (kg m ⁻³)	6.6 · 10 ¹⁵	1.6 · 10 ¹⁵
O ₂ ⁺ density (m ⁻³)	1.2 · 10 ¹¹	1.2 · 10 ¹¹
O ⁺ density (m ⁻³)	4.7 · 10 ⁷	5.5 · 10 ⁷
<i>h = 150 km</i>		
Electron density (m ⁻³)	9.5 · 10 ¹⁰	8.3 · 10 ¹⁰
Neutral temperature (K)	258.3	254.6
Electron temperature (K)	282.8	262.5
Magnetic field (nT)	0	9.9
CO ₂ density (kg m ⁻³)	5.9 · 10 ¹⁵	4.8 · 10 ¹⁵
O ₂ density (kg m ⁻³)	2.2 · 10 ¹³	2.2 · 10 ¹³
O density (kg m ⁻³)	2.8 · 10 ¹⁵	6.9 · 10 ¹⁴
O ₂ ⁺ density (m ⁻³)	9.3 · 10 ¹⁰	7.8 · 10 ¹⁰
O ⁺ density (m ⁻³)	1.2 · 10 ⁸	1.1 · 10 ⁸
<i>h = 170 km</i>		
Electron density (m ⁻³)	6.2 · 10 ¹⁰	4.9 · 10 ¹⁰
Neutral temperature (K)	300.0	284.4
Electron temperature (K)	375.1	303.2
Magnetic field (nT)	0	14.6
CO ₂ density (kg m ⁻³)	1.5 · 10 ¹⁵	1.2 · 10 ¹⁵
O ₂ density (kg m ⁻³)	5.5 · 10 ¹²	5.5 · 10 ¹²
O density (kg m ⁻³)	1.3 · 10 ¹⁵	3.4 · 10 ¹⁴
O ₂ ⁺ density (m ⁻³)	6.0 · 10 ¹⁰	4.5 · 10 ¹⁰
O ⁺ density (m ⁻³)	2.0 · 10 ⁸	1.5 · 10 ⁸
<i>h = 200 km</i>		
Electron density (m ⁻³)	3.4 · 10 ¹⁰	2.2 · 10 ¹⁰
Neutral temperature (K)	331.8	299.7
Electron temperature (K)	535.5	353.0
Magnetic field (nT)	0	20.7
CO ₂ density (kg m ⁻³)	2.2 · 10 ¹⁴	1.6 · 10 ¹⁴
O ₂ density (kg m ⁻³)	7.9 · 10 ¹¹	7.4 · 10 ¹¹
O density (kg m ⁻³)	6.2 · 10 ¹⁴	1.6 · 10 ¹⁴
O ₂ ⁺ density (m ⁻³)	3.2 · 10 ¹⁰	2.0 · 10 ¹⁰
O ⁺ density (m ⁻³)	4.1 · 10 ⁸	2.3 · 10 ⁸

^aMEX = Mars Express.

characteristics. In black, seven profiles from Mars Express orbit 4210 (Period A) and in red, seven profiles from Mars Express orbit 6592 (Period B). Both sets of profiles have practically the same conditions: SZA between 45 and 55°; a heliocentric distance of 1.40 AU; latitudes of -40 and -63°, respectively; longitudes of 73 and 327°E, respectively; solar longitudes of 220 and 213°, respectively (spring); 69 solar flux unit of $F_{10.7}$ index as a proxy of EUV radiation; and $1.5 \cdot 10^{-4} \text{ W/m}^2/\text{nm}$ for the 30.5 nm wavelength of the EUV solar irradiance at Mars (see Figure 1). As in the previous figures, profiles are located over areas where the crustal magnetic field is negligible [Cain *et al.*, 2003]. In principle, since the conditions for ionospheric formation are equivalent, both orbits should yield similar results. Indeed, the peak characteristics (altitude and electron density) are practically the same for both cases. The neutral scale height at the altitude of the peak electron density of both orbits is on average 10.5 km, which implies a temperature of the neutral population around 190 K (calculated with equation (1)). This suggests that the density of the neutral atmosphere at that height was quite similar for these cases, since the peak altitude is directly proportional to the neutral density of the atmosphere [Schunk and Nagy, 2009]. Nevertheless, the first important difference is that the electron density of the red profiles at higher altitudes is smaller, suggesting additional ionospheric cooling for this case despite

having, in principle, the same level of solar radiation. The second important difference is the transition altitude (sudden change of slope) found at 180 km in the red profiles, which is interpreted as being the lowest altitude at which the induced magnetic field has a significant influence.

Although Mars Express does not have a magnetometer, the magnetic field magnitude at the spacecraft location can be derived from the MARSIS instrument under certain circumstances [Gurnett *et al.*, 2008; Akalin *et al.*, 2010]. For the orbit 6592 (in red, low solar activity), MARSIS recorded a clear magnetic field value of 26 nT at the spacecraft altitude in the seven profiles, during which the spacecraft altitude barely changed, while no estimates of the magnetic field were available for orbit 4210. Note that the lack of a magnetic measurement at the spacecraft position does not mean an absence of a field. This observed magnetic field allows us to set up the upper boundary condition at 500 km altitude needed in the numerical model to compute the vertical profile of the magnetic field. The lower boundary condition is set at 0 nT at 100 km altitude. The resulting profile of the magnetic field is displayed in Figure 5. The model was run for each data set for the conditions of each date (Table 2), while a magnetic field of magnitude 26 nT at 370 km of altitude was used for orbit 6592, and a value of 0 nT for orbit 4210. Figure 5a shows the simulated electron density

profiles (dashed lines), the induced magnetic field profile used in one simulation (dash-dotted line), the neutral and electron temperatures (Figure 5b), the O^+ and O_2^+ density profiles (Figure 5c), and the vertical O_2^+ ion velocities (Figure 5d) derived from the simulations.

Although the numerical solution is not unique since the run was based on a single value of magnetic field and the behavior of the red profiles is less constant than the black ones, the electron density simulations reproduce the slope of both sets of profiles. It indicates that the induced magnetic field scenario for the low solar activity case is reasonable. Indeed, the simulated magnetic field profile is in good agreement with the magnetic field profiles measured by MGS in the previous solar cycle [Opgenoorth *et al.*, 2010, Figure 6]. For almost the same neutral scale height at the peak, the slope of the topside profiles is smaller for orbit 6592 (Period B). This means that the plasma pressure of the ionosphere for that case was smaller, as can also be observed from the smaller electron temperature between 150 and 250 km (Figure 5b). Thus, the simulations indicate a cooler ionosphere for the low solar activity case: 16 K and 72 K lower for the neutral and electron temperatures, respectively, at 35 km above the peak (which is at 135 km); 22 K and 113 K lower at 45 km above the peak; and 32 K and 183 K lower at 65 km above the peak. This produces the observed reduction in the density, as suggested above. Indeed, the average neutral temperature difference at 40 km from the peak is about 20 K in the simulations, which is the same result found in Table 1 for Periods A and B with equation (1). There is a transition in the electron density profile which starts at about 180 km, the limit between the photochemical and diffusion region for the red profiles. As observed in the vertical ion velocity panel, for the red profiles, the photochemical region (velocity close to zero) finished at this altitude, leading to a downward ion velocity associated with the penetration of the magnetic field in the ionosphere. The electron temperature becomes higher at altitudes above 250 km due to lower thermal conductivities. On the contrary, the diffusion region starts at about 220 km for the unmagnetized case, having first a small negative incursion of the velocity, mostly due to ion thermal diffusion, and then an upward plasma velocity, which is explained by the change in which O^+ became the major ion (Figure 5c).

5. Summary

Solar cycle variations create changes in the topside ionosphere of Mars. The Mars Express MARSIS AIS data set, within the SZA interval of 45–55°, was split into four periods according to notable changes in the solar spectrum (Figure 1). A singular behavior is observed for low and high solar activity phases, which do not respond in the same way to changes in the EUV flux at Mars (the main factor of ionization). Specifically, the low solar activity phase (Period B) differs from the other periods as the topside electron density does not show any apparent dependence on this radiation, while during the high solar activity phase, the topside density profile was larger. The absence of X-ray flux during the low solar activity period may have played a major role, although this radiation is typically associated with the formation of the ionospheric secondary layer (~110 km of altitude).

In general, the Martian topside ionosphere observations are better reproduced with a neutral scale height that increases linearly with altitude, except for the case of the low solar activity phase (Figures 3 and 4). In this latter case, there is evidence for either a constant scale height or a height-variable scale height with lower electron density. During that phase, the ionospheric temperature was cooler, and therefore, the electron density and scale height were smaller than in other phases of the solar cycle, resulting in a reduced plasma pressure. Simulations made with the numerical/fluid model TRANSMARS (Figure 5) indicate that most probably, the induced solar wind magnetic field penetrated more easily into the ionosphere, leading to a larger compression of the topside than in other phases of the solar cycle.

All the available evidence seems to indicate that as for Earth, the deep and long recent solar minimum created a colder thermosphere with lower density, and therefore, an exceptional behavior in the response of the Mars' ionosphere was found. Despite the substantial geophysical differences between Mars and Earth, the vertical structure of their dayside ionospheres seems to respond similarly to solar cycle variability.

References

- Acuña, M. H., *et al.* (1999), Global distribution of crustal magnetization discovered by the Mars Global Surveyor MAG/ER Experiment, *Science*, 285(5415), 790–793, doi:10.1126/science.284.5415.790.
- Adewale, A. O., E. O. Oyeyemi, P. J. Cilliers, L. A. McKinnell, and A. B. Adelaye (2012), Low solar activity variability and IRI 2007 predictability of equatorial Africa GPS TEC, *Adv. Space Res.*, 49, 316–326, doi:10.1016/j.asr.2011.09.032.

Acknowledgments

B.S.-C., M.L., and S.E.M. acknowledge support through STFC grant ST/K001000/1 and BESH through the STFC ST/K502121/1. B.S.-C. acknowledges a scientific stay at ESA-ESTEC by ESTEC Faculty support funding. Authors acknowledge MARSIS PIs for making data accessible. The Mars Express MARSIS AIS data were downloaded from the ESA Planetary Science Archive (<http://www.rssd.esa.int/psa>) and the solar flux data from NOAA service (<ftp://ftp.swpc.noaa.gov/pub/warehouse/>) and University of Colorado's website (<http://lasp.colorado.edu/lisird/index.html>). The authors acknowledge the two reviewers for improving this work.

- Akalin, F., D. D. Morgan, D. A. Gurnett, D. L. Kirchner, D. A. Brain, R. Modolo, M. H. Acuña, and J. R. Espley (2010), Dayside induced magnetic field in the ionosphere of Mars, *Icarus*, *206*, 104–111, doi:10.1016/j.icarus.2009.03.021.
- Andrews, D. J., H. J. Opgenoorth, N. J. T. Edberg, M. Andre, M. Franz, E. Dubinin, F. Duru, D. Morgan, and O. Witasse (2013), Determination of local plasma densities with the MARSIS radar: Asymmetries in the high-altitude Martian ionosphere, *J. Geophys. Res. Space Physics*, *118*, 6228–6242, doi:10.1002/jgra.50593.
- Belehaki, A., P. Marinov, I. Kutiev, N. Jakowski, and S. Stankov (2006), Comparison of the topside ionosphere scale height determined by topside sounders model and bottomside digisonde profiles, *Adv. Space Res.*, *37*, 963–966, doi:10.1016/j.asr.2005.09.014.
- Billitz, D., and B. W. Reinisch (2008), International Reference Ionosphere 2007: Improvements and new parameters, *Adv. Space Res.*, *43*, 599–609, doi:10.1016/j.asr.2007.07.048.
- Blelly, P.-L., J. Liliensten, A. Robineau, J. Fontanari, and D. Alcayde (1996), Calibration of a numerical ionospheric model with EISCAT observations, *Ann. Geophys.*, *14*, 1375–1390.
- Bougher, S. W., S. Engel, D. P. Hinson, and J. M. Forbes (2001), Mars Global Surveyor Radio Science electron density profiles: Neutral atmosphere implications, *Geophys. Res. Lett.*, *28*, 3091–3094.
- Bougher, S. W., D. Pawlowski, J. M. Bell, S. Nelli, T. McDunn, J. R. Murphy, M. Chizek, and A. Ridley (2015), Mars Global Ionosphere-Thermosphere Model (MGITM): Solar cycle, seasonal, and diurnal variations of the Mars upper atmosphere, *J. Geophys. Res. Planets*, *120*, 311–342, doi:10.1002/2014JE004715.
- Cain, J. C., B. B. Ferguson, and D. Mozzoni (2003), An $n = 90$ internal potential function of the Martian crustal magnetic field, *J. Geophys. Res.*, *108*(E2), 5008, doi:10.1029/2000JE001487.
- Chicarro, A., P. Martin, and R. Traunter (2004), *Mars Express: A European Mission to the Red Planet* SP-1240, pp. 3–16, Eur. Space Agency Publ. Div., Noordwijk, Netherlands.
- Cravens, T. E. (1997), *Physics of Solar System Plasmas*, Cambridge Univ. Press, Cambridge, U. K.
- Culot, F., C. Lathuillere, J. Liliensten, and O. Witasse (2004), The OI 630 nm and 557.7 nm dayglow measured by WINDII and modeled by TRANSCAR, *Ann. Geophys.*, *22*, 1947–1960.
- Diloy, P.-Y., A. Robineau, J. Liliensten, P.-L. Blelly, and J. Fontanari (1996), A numerical model of the ionosphere, including the E-region above EISCAT, *Ann. Geophys.*, *14*, 191–200.
- Dubinin, E., et al. (2008), Structure and dynamics of the solar wind/ionosphere interface on Mars: MEX-ASPERA-3 and MEX-MARSIS observations, *Geophys. Res. Lett.*, *35*, L11103, doi:10.1029/2008GL033730.
- Fox, J. L., P. Zhou, and S. W. Bougher (1996), The thermosphere/ionosphere of Mars at high and low solar activities, *Adv. Space Res.*, *17*(11), 203–218.
- Grubb, R. N. (1975), The SMS/GOES space environment monitor subsystem, NOAA Tech. Mem. SEL-42, Space Environ. Lab., Boulder, Colo.
- Gurnett, D. A., et al. (2005), Radar soundings of the ionosphere of Mars, *Science*, *310*, 1999–1933, doi:10.1126/science.1121868.
- Gurnett, D. A., et al. (2008), An overview of radar soundings of the Martian ionosphere from the Mars Express spacecraft, *Adv. Space Res.*, *41*, 1335–1346, doi:10.1016/j.asr.2007.01.062.
- Halekas, J. S., et al. (2015), MAVEN observations of solar wind hydrogen deposition in the atmosphere of Mars, *Geophys. Res. Lett.*, *42*, doi:10.1002/2015GL064693.
- Hanson, W. B., S. Sanatani, and D. R. Zuccaro (1977), The Martian ionosphere as observed by the Viking retarding potential analyzers, *J. Geophys. Res.*, *82*(28), 4351–4363.
- Hinson, D. P., R. A. Simpson, J. D. Twicken, G. L. Tyler, and F. M. Flasar (1999), Initial results from radio occultation measurements with Mars Global Surveyor, *J. Geophys. Res.*, *104*, 26,997–27,012.
- Kieffer, H. H., B. M. Jakosky, C. W. Snyder, and M. S. Matthews (1992), *Mars*, The Univ. of Ariz. Press, Tucson.
- Klenzing, J., F. Simoes, S. Ivanov, D. Billitz, R. A. Heelis, and D. Rowland (2013), Performance of the IRI-2007 model for equatorial topside ion density in the African sector for low and extremely low solar activity, *Adv. Space Res.*, *52*, 1780–1790, doi:10.1016/j.asr.2012.09.030.
- Leblanc, F., et al. (2008), Observations of aurorae by SPICAM ultraviolet spectrograph on board Mars Express: Simultaneous ASPERA-3 and MARSIS measurements, *J. Geophys. Res.*, *113*, A08311, doi:10.1029/2008JA013033.
- Leblanc, F., et al. (2015), Mars heavy ion precipitating flux as measured by Mars Atmosphere and Volatile Evolution, *Geophys. Res. Lett.*, *42*, doi:10.1002/2015GL066170.
- Liliensten, J., W. Kofman, J. Wisemberg, E. S. Oran, and C. R. Devore (1989), Ionization efficiency due to primary and secondary photoelectrons—A numerical model, *Ann. Geophys.*, *7*, 83–90.
- Lillis, R. J., D. A. Brain, S. L. England, P. Withers, M. O. Fillingim, and A. Safaeinili (2010), Total electron content in the Mars ionosphere: Temporal studies and dependence on solar EUV flux, *J. Geophys. Res.*, *115*, A11314, doi:10.1029/2010JA015698.
- Lillis, R. J., D. A. Brain, G. T. Delory, D. L. Mitchell, J. G. Luhmann, and R. P. Lin (2012), Evidence for superthermal secondary electrons produced by SEP ionization in the Martian atmosphere, *J. Geophys. Res.*, *117*, E03004, doi:10.1029/2011JE003932.
- Luhmann, J. G., C. T. Russel, L. H. Brace, and O. L. Vaisberg (1992), The intrinsic magnetic field and solar-wind interaction of Mars, in *Mars*, pp. 1090–1134, The Univ. of Ariz. Press, Tucson.
- Mendillo, M., P. Withers, D. Hinson, H. Rishbeth, and B. Reinisch (2006), Effects of solar flares on the ionosphere of Mars, *Science*, *311*, 1135–1138.
- Morel, L., O. Witasse, R. Warnant, J.-C. Cerisier, P.-L. Blelly, and J. Liliensten (2004), Diagnostic of the dayside ionosphere of Mars using the total electron content measurement by the NEIGE/Netlander experiment: An assessment study, *Planet. Space Sci.*, *52*(7), 603–611, doi:10.1016/j.pss.2003.12.007.
- Morgan, D. D., O. Witasse, E. Nielsen, D. A. Gurnett, F. Duru, and D. L. Kirchner (2013), The processing of electron density profiles from the Mars Express MARSIS topside sounder, *Radio Sci.*, *48*, 197–207, doi:10.1002/rds.20023.
- Nava, B., P. Coisson, and S. M. Radicella (2008), A new version of the NeQuick ionosphere electron density model, *J. Atmos. Sol. Terr. Phys.*, *70*, 1856–1862, doi:10.1016/j.jastp.2008.01.015.
- Ness, N. F., M. H. Acuña, J. E. P. Connerney, A. J. Kliore, T. K. Breus, A. M. Krymskii, P. Cloutier, and S. J. Bauer (2000), Effects of magnetic anomalies discovered at Mars on the structure of the Martian ionosphere and solar wind interaction as follows from radio occultation experiments, *J. Geophys. Res.*, *105*, 15,991–16,004.
- Opgenoorth, H. J., R. S. Dhillon, L. Rosenqvist, M. Lester, N. J. T. Edberg, S. E. Milan, P. Withers, and D. Brain (2010), Day-side ionospheric conductivities at Mars, *Planet. Space Sci.*, *58*, 1139–1151, doi:10.1016/j.pss.2010.04.004.
- Picardi, G., et al. (2004), *Mars Express: A European Mission to the Red Planet*, MARSIS: Mars Advanced Radar for Subsurface and Ionosphere Sounding SP-1240, pp. 51–70, Eur. Space Agency Publ. Div., Noordwijk, Netherlands.
- Richards, P. G., J. A. Fennelly, and D. G. Torr (1994), EUVAC: A solar EUV flux model for aeronomical calculations, *J. Geophys. Res.*, *99*, 8981–8992.
- Russell, C. T., and O. Vaisberg (1983), The interaction of the solar wind with Venus, in *Venus*, edited by D. M. Hunten et al., 873 pp., The Univ. of Ariz. Press, Tucson.

- Sánchez-Cano, B., O. Witasse, M. Herraiz, S. M. Radicella, J. Bauer, P.-L. Blelly, and G. Rodríguez-Caderot (2012), Retrieval of ionospheric profiles from the Mars Express MARSIS experiment data and comparison with radio-occultation data, *Geosci. Instrum. Method Data Syst.*, *1*, 77–84, doi:10.5194/gi-1-77-2012.
- Sánchez-Cano, B., S. M. Radicella, M. Herraiz, O. Witasse, and G. Rodríguez-Caderot (2013), NeMars: An empirical model of the Martian dayside ionosphere based on Mars Express MARSIS data, *Icarus*, *225*, 236–247, doi:10.1016/j.icarus.2013.03.021.
- Sánchez-Cano, B., et al. (2015), Total electron content in the Martian atmosphere: A critical assessment of the Mars Express MARSIS data sets, *J. Geophys. Res. Space Physics*, *120*, 2166–2182, doi:10.1002/2014JA020630.
- Schunk, R., and A. F. Nagy (2009), *Ionospheres: Physics, Plasma Physics, and Chemistry*, Cambridge Univ. Press, New York.
- Sethi, N. K., R. S. Dabas, and S. K. Sarkar (2011), Validation of IRI-2007 against TEC observations during low solar activity over Indian sector, *J. Atmos. Sol. Terr. Phys.*, *73*, 751–759, doi:10.1016/j.jastp.2011.02.011.
- Shinagawa, H., and T. E. Cravens (1989), A one-dimensional multispecies magnetohydrodynamic model of the dayside ionosphere of Mars, *J. Geophys. Res.*, *94*, 6506–6516.
- Simon, C., J. Liliensten, O. Dutuit, R. Thissen, O. Witasse, C. Alcaraz, and H. Soldi-Lose (2005), Prediction and modelling of doubly-charged ions in the Earth's upper atmosphere, *Ann. Geophys.*, *23*(3), 781–797.
- Simon, C., O. Witasse, F. Leblanc, G. Gronoff, and J.-L. Bertaux (2009), Dayglow on Mars: Kinetic modelling with SPICAM UV limb data, *Planet. Space Sci.*, *57*, 1008–1021.
- Solomon, S. C., T. N. Woods, L. V. Didkovsky, J. T. Emmert, and L. Qian (2010), Anomalous low solar extreme-ultraviolet irradiance and thermospheric density during solar minimum, *Geophys. Res. Lett.*, *37*, L16103, doi:10.1029/2010GL044468.
- Solomon, S. C., L. Qian, L. V. Didkovsky, R. A. Viereck, and T. N. Woods (2011), Causes of low thermospheric density during the 2007–2009 solar minimum, *J. Geophys. Res.*, *116*, A00H07, doi:10.1029/2011JA016508.
- Solomon, S. C., L. Qian, and A. G. Burns (2013), The anomalous ionosphere between solar cycle 23 and 24, *J. Geophys. Res. Space Physics*, *118*, 6524–6535, doi:10.1002/jgra.50561.
- Witasse, O. (2000), *Modélisation des Ionosphères planétaires et de leur Rayonnement: La Terre et Mars*, PhD thesis, Laboratoire de Planétologie de Grenoble.
- Witasse, O., J. Liliensten, C. Lathuillère, and P.-L. Blelly (1999), Modeling the OI 630.0 and 557.7 nm thermospheric dayglow during EISCAT-WINDII coordinated measurements, *J. Geophys. Res.*, *104*, 24,639–24,656.
- Witasse, O., et al. (2002), Prediction of a CO₂⁺ layer in the atmosphere of Mars, *Geophys. Res. Lett.*, *29*(8), 1263, doi:10.1029/2002GL014781.
- Witasse, O., et al. (2003), Correction to “Prediction of a CO₂⁺ layer in the atmosphere of Mars”, *Geophys. Res. Lett.* *30*(7), 1360, doi:10.1029/2003GL017007.
- Witasse, O., T. Cravens, M. Mendiola, J. Moses, A. Kliore, F. Nagy, and T. Breus (2008), Solar system ionospheres, *Space Sci. Rev.*, *139*, 235–265, doi:10.1007/s11214-008-9395-3.
- Withers, P. (2009), A review of observed variability in the dayside ionosphere of Mars, *Adv. Space Res.*, *44*, 277–307, doi:10.1016/j.asr.2009.04.027.
- Withers, P., et al. (2012), A clear view of the multifaceted dayside ionosphere of Mars, *Geophys. Res. Lett.*, *39*, L18202, doi:10.1029/2012GL053193.
- Withers, P., D. D. Morgan, and D. A. Gurnett (2014), Variations in peak electron densities in the ionosphere of Mars over a full solar cycle, *Icarus*, *251*, 5–11, doi:10.1016/j.icarus.2014.08.008.
- Woods, T. N., and F. G. Eparvier (2006), Solar ultraviolet variability during the TIMED mission, *Adv. Space Res.*, *37*, 219–224, doi:10.1016/j.asr.2004.10.006.
- Yue, X., W. S. Schreiner, C. Rocken, and Y.-H. Kuo (2013), Validate the IRI2007 model by the COSMIC slant TEC data during the extremely solar minimum of 2008, *Adv. Space Res.*, *51*, 647–653, doi:10.1016/j.asr.2011.08.011.
- Zhang, M. H. G., and J. G. Luhmann (1992), Comparisons of peak ionosphere pressures at Mars and Venus with incident solar wind dynamic pressure, *J. Geophys. Res.*, *97*, 1017–1025.